

Data-Guided Physics-Informed Neural Networks for Solving Inverse Problems in Partial Differential Equations

Wei Zhou^{a,*}, Y.F. Xu^a

^a*Department of Mechanical and Materials Engineering, University of Cincinnati, Cincinnati, OH 45221, USA*

Abstract

Physics-informed neural networks (PINNs) represent a significant advancement in scientific machine learning by integrating fundamental physical laws into their architecture through loss functions. PINNs have been successfully applied to solve various forward and inverse problems in partial differential equations (PDEs). However, a notable challenge can emerge during the early training stages when solving inverse problems. Specifically, data losses remain high while PDE residual losses are minimized rapidly, thereby exacerbating the imbalance between loss terms and impeding the overall efficiency of PINNs. To address this challenge, this study proposes a novel framework termed data-guided physics-informed neural networks (DG-PINNs). The DG-PINNs framework is structured into two distinct phases: a pre-training phase and a fine-tuning phase. In the pre-training phase, a loss function with only the data loss is minimized in a neural network. In the fine-tuning phase, a composite loss function, which consists of the data loss, PDE residual loss, and, if available, initial and boundary condition losses, is minimized in the same neural network. Notably, the pre-training phase ensures that the data loss is already at a low value before the fine-tuning phase commences. This approach enables the fine-tuning phase to converge to a minimal composite loss function with fewer iterations compared to existing PINNs. To validate the effectiveness, noise-robustness, and efficiency of DG-PINNs, extensive numerical investigations are conducted on inverse problems related to several classical PDEs, including the heat equation, wave equation, Euler–Bernoulli beam equation, and Navier–Stokes equation. The numerical results demonstrate that DG-

*Corresponding author

Email addresses: zhouw6@mail.uc.edu (Wei Zhou), yongfengxuyf@gmail.com (Y.F. Xu)

PINNs can accurately solve these inverse problems and exhibit robustness against noise in training data. Furthermore, it is shown that DG-PINNs can significantly enhance the efficiency in solving inverse problems compared to existing PINNs while maintaining high solution accuracy. For transparency and reproducibility, all codes and datasets used in this study are freely available at <https://github.com/dopawei/DG-PINNs>.

Keywords: Data-guided physics-informed neural networks; Physics-informed neural networks; Inverse problems; Partial differential equations; Scientific machine learning

1. Introduction

In recent years, physics-informed machine learning [1], particularly physics-informed neural networks (PINNs) [2], has become a promising method for solving complex problems involving partial differential equations (PDEs). PINNs leverage the universal approximation capabilities of neural networks [3] and automatic differentiation [4] to approximate the latent solutions of PDEs. The fundamental physical laws are integrated into loss functions of neural networks through automatic differentiation [2]. This integration can be traced back to the 1990s [5, 6, 7], which enables neural network outputs to comply with fundamental physical laws. PINNs have been applied to a diverse range of fields, including fluid dynamics [8, 9, 10, 11], continuum mechanics [12, 13, 14, 15], biomedical engineering [16], and others [17, 18, 19, 20].

Despite the broad applicability of PINNs, several challenges remain in training PINNs efficiently and effectively. Issues such as imbalanced gradient magnitudes of loss terms [21] and inherent spectral biases [22, 23] within PINNs can impede convergence and result in poor solutions [24, 25]. Recent efforts have focused on enhancing the trainability of PINNs. Specifically, for the challenge of imbalanced gradient magnitudes, Wang et al. [21] have identified this as a significant factor in the failure of PINNs. They proposed a learning rate annealing algorithm as a solution to balance gradient magnitudes of loss terms. Besides, Wang et al. [25] explored the training dynamics of PINNs through the lens of the neural tangent kernel (NTK) theory [26] and found a notable discrepancy in the convergence rate of each loss term. They introduced a novel adaptive weights algorithm that utilizes the eigenvalues of the NTK to adaptively adjust loss weights.

Furthermore, Li et al. [27] observed that not only gradient magnitudes of loss terms are often imbalanced, but also the gradient directions of loss terms are usually conflicting. To address both issues, they introduced an adaptive gradient descent method for balancing gradient magnitudes and eliminating conflicts in gradient directions. For the challenge of inherent spectral biases in PINNs, approaches such as Fourier feature networks [28] have been applied for PDEs involving high-frequency components in their latent solutions [24, 29]. Additionally, several methods have been proposed to enhance the training efficiency and performance of PINNs, including sinusoidal input mapping [30], residual-based adaptive refinement [31], the coupled-automatic-numerical differentiation framework [32], and other variants of PINNs [33, 34, 35, 36, 37].

In solving inverse problems using existing PINNs, the primary objective is to accurately estimate unknown parameters within PDEs from observed data. To achieve this objective, PINNs are trained to minimize a composite loss function, which includes the PDE residual loss, initial condition loss, boundary condition loss and data loss [2, 9, 12, 38, 39, 40, 41, 14]. For instance, Mao et al. [9] employed PINNs to estimate density, velocity, and pressure fields for one-dimensional Euler equations from observed density gradient data. Besides, Rasht et al. [40] applied PINNs for full waveform inversions in seismic imaging to estimate the wave speed from observed data. It is noted that the data loss is derived from neural network outputs, while the PDE residual loss is based on both derivatives of these neural network outputs and unknown parameters within PDEs. Besides, initial neural network outputs in PINNs tend to approximate flat output functions, which can be governed by numerous PDEs [30]. Hence, during the early stages of training PINNs, the PDE residual loss can be minimized to a negligible level, yet the data loss remains at a high level. This imbalance between the loss terms requires additional training iterations to both reduce the data loss and accurately estimate unknown parameters, thus impeding the efficiency of solving inverse problems by PINNs.

To address the challenge of solving inverse problems with PINNs, this paper introduces a novel framework termed data-guided physics-informed neural networks (DG-PINNs).

The DG-PINNs framework consists of two phases. The first phase is the pre-training phase: a neural network is trained to minimize the data loss. The second phase is the fine-tuning phase: the neural network is further optimized to simultaneously minimize the composite loss function. To assess the effectiveness, noise-robustness, and efficiency of DG-PINNs, extensive numerical investigations are conducted on various PDEs, including the heat equation, wave equation, Euler–Bernoulli beam equation, and Navier–Stokes equation. For each equation, sensitivity analyses of the DG-PINNs results are conducted, focusing on two hyperparameters: the maximum number of iterations in the pre-training phase and the number of data points in training datasets for the data loss. Besides, a comparative analysis between DG-PINNs and PINNs is conducted for each investigated equation.

The paper is organized as follows: Sections 2.1 through 2.3 provide a brief overview of the fundamentals of fully-connected neural networks, PINNs for inverse problems, and the adaptive weights algorithm, respectively. Section 2.4 details the proposed DG-PINNs. Section 3 presents extensive numerical investigations, illustrating the effectiveness, noise-robustness and efficiency of DG-PINNs in various inverse problems. Finally, Section 4 offers concluding remarks and future research directions.

2. Methodology

2.1. Fully-connected neural networks

Consider a H -layer fully connected feed-forward neural network, which consists of H hidden layers. This neural network can be expressed in a recurrent form as follows:

$$\mathbf{f}^{(h)} = \sigma(\mathbf{W}^{(h)}\mathbf{f}^{(h-1)} + \mathbf{b}^{(h)}), \quad h = 1, 2, \dots, H, \quad (1)$$

where $\mathbf{f}^{(h)}$ denotes the output of the h -th hidden layer, $\mathbf{f}^{(0)}$ is the neural network input, $\sigma(\cdot)$ is the nonlinear activation function, $\mathbf{W}^{(h)}$ and $\mathbf{b}^{(h)}$ denote the weight matrix and bias vector for the h -th hidden layer, respectively. The neural network output is given by

$$\hat{\mathbf{u}} = \mathbf{W}^{(H+1)}\mathbf{f}^{(H)} + \mathbf{b}^{(H+1)}, \quad (2)$$

where $\mathbf{W}^{(H+1)}$ and $\mathbf{b}^{(H+1)}$ are the weight matrix and bias vector of the output layer, respectively. The set of all parameters, including weights and biases within the network, can be grouped and denoted by

$$\boldsymbol{\theta} = \{\mathbf{W}^{(1)}, \mathbf{b}^{(1)}, \dots, \mathbf{W}^{(h)}, \mathbf{b}^{(h)}, \dots, \mathbf{W}^{(H+1)}, \mathbf{b}^{(H+1)}\}. \quad (3)$$

The architecture of this neural network integrates linear operations with nonlinear activation functions. When the activation functions are infinitely differentiable, such as sine, cosine, and hyperbolic functions, this architecture allows the computation of meaningful derivatives of any order for the output $\hat{\mathbf{u}}$ with respect to the neural network input through the automatic differentiation [4]. Such derivatives facilitate the integration of fundamental physical laws into loss functions in PINNs.

2.2. PINNs for solving inverse problems

PINNs offer a novel method for solving inverse problems in PDEs of various systems. Such a typical inverse problem is formulated as

$$\mathcal{F}[u(\mathbf{x}, t); \boldsymbol{\gamma}] = s(\mathbf{x}, t), \quad \mathbf{x} \in \Omega, t \in [0, T], \quad (4)$$

where $\mathcal{F}[\cdot]$ is the differential operator, $u(\mathbf{x}, t)$ denotes the observed data, $\mathbf{x} = [x_1, \dots, x_n]$ is the spatial coordinates, t is the time variable over the duration T , $\boldsymbol{\gamma}$ are parameters related to the physics of the system, all or some of which are unknown parameters for inverse problems, and $s(\mathbf{x}, t)$ is the source function. The initial conditions of Eq. (4) can be expressed by

$$\mathcal{I}[u(\mathbf{x}, t)] = f(\mathbf{x}), \quad \mathbf{x} \in \Omega, t = 0, \quad (5)$$

and the boundary condition of Eq. (4) can be expressed by

$$\mathcal{B}[u(\mathbf{x}, t)] = q(\mathbf{x}, t), \quad \mathbf{x} \in \partial\Omega, t \in [0, T], \quad (6)$$

where $\mathcal{I}[\cdot]$ and $f(\mathbf{x})$ denote the initial condition operator and initial condition function, respectively, and $\mathcal{B}[\cdot]$ and $q(\mathbf{x}, t)$ denote the boundary condition operator and boundary condition function, respectively.

For solving inverse problems using PINNs, the aim is to accurately estimate γ . To achieve this aim, PINNs are trained to minimize a composite loss function [2], which is expressed by

$$\mathcal{L}(\Theta) = \lambda_r \mathcal{L}_r(\Theta) + \lambda_i \mathcal{L}_i(\theta) + \lambda_b \mathcal{L}_b(\theta) + \lambda_d \mathcal{L}_d(\theta), \quad (7)$$

where $\Theta = \{\theta, \gamma\}$ with the total number of parameters M , λ_r , λ_i , λ_b and λ_d are loss weights corresponding to the PDE residual loss $\mathcal{L}_r(\Theta)$, initial condition loss $\mathcal{L}_i(\theta)$, boundary condition loss $\mathcal{L}_b(\theta)$, and data loss $\mathcal{L}_d(\theta)$, respectively. With the prediction of PINNs, $\hat{u}(\mathbf{x}, t; \theta)$, the aforementioned individual loss terms are expressed by

$$\mathcal{L}_r(\Theta) = \frac{1}{N_r} \sum_{k=1}^{N_r} (\mathcal{F}[\hat{u}(\mathbf{x}_r^k, t_r^k; \theta); \gamma] - s(\mathbf{x}_r^k, t_r^k))^2, \quad (8)$$

$$\mathcal{L}_i(\theta) = \frac{1}{N_i} \sum_{k=1}^{N_i} (\mathcal{I}[\hat{u}(\mathbf{x}_i^k, t_i^k; \theta)] - f(\mathbf{x}_i^k))^2, \quad (9)$$

$$\mathcal{L}_b(\theta) = \frac{1}{N_b} \sum_{k=1}^{N_b} (\mathcal{B}[\hat{u}(\mathbf{x}_b^k, t_b^k; \theta)] - q(\mathbf{x}_b^k, t_b^k))^2, \quad (10)$$

and

$$\mathcal{L}_d(\theta) = \frac{1}{N_d} \sum_{k=1}^{N_d} (\hat{u}(\mathbf{x}_d^k, t_d^k; \theta) - u(\mathbf{x}_d^k, t_d^k))^2, \quad (11)$$

where N_r , N_i , N_b and N_d are the number of data points in training datasets $\{\mathbf{x}_r^k, t_r^k, s(\mathbf{x}_r^k, t_r^k)\}_{k=1}^{N_r}$, $\{\mathbf{x}_i^k, t_i^k, f(\mathbf{x}_i^k)\}_{k=1}^{N_i}$, $\{\mathbf{x}_b^k, t_b^k, q(\mathbf{x}_b^k, t_b^k)\}_{k=1}^{N_b}$, and $\{\mathbf{x}_d^k, t_d^k, u(\mathbf{x}_d^k, t_d^k)\}_{k=1}^{N_d}$, respectively. In this context, \mathbf{x}_j^k and t_j^k for $j = r, i, b$, and d , denote discrete spatial coordinates and discrete time points for the k -th data point in each dataset, respectively. The minimizer of $\mathcal{L}(\Theta)$ can be expressed by

$$\Theta^* = \arg \min_{\Theta} \mathcal{L}(\Theta), \quad (12)$$

where $\Theta^* = \{\theta^*, \gamma^*\}$ with θ^* and γ^* being the optimal parameters and the estimated unknown parameters, respectively, and $\arg \min(\cdot)$ is the arguments of the minimum. A schematic illustration of PINNs for solving inverse problems is provided in Fig. 1. It is noted that the neural network inputs, $\mathbf{x}_1, \dots, \mathbf{x}_n$, and \mathbf{t} are collections of the spatial coordinate components and time values, respectively, from various training datasets. Specifically, \mathbf{x}_j collects the j -th spatial coordinate from training datasets as $\mathbf{x}_j = \left\{ (x_j)_r^k \right\}_{k=1}^{N_r} \cup \left\{ (x_j)_i^k \right\}_{k=1}^{N_i} \cup \left\{ (x_j)_b^k \right\}_{k=1}^{N_b} \cup \left\{ (x_j)_d^k \right\}_{k=1}^{N_d}$. Similarly, \mathbf{t} collects the time values from these datasets as $\mathbf{t} = \left\{ t_r^k \right\}_{k=1}^{N_r} \cup \left\{ t_i^k \right\}_{k=1}^{N_i} \cup \left\{ t_b^k \right\}_{k=1}^{N_b} \cup \left\{ t_d^k \right\}_{k=1}^{N_d}$. The neural network output, $\hat{\mathbf{u}}$, is formulated as $\hat{\mathbf{u}} = \left\{ \hat{u}(\mathbf{x}_r^k, t_r^k; \theta) \right\}_{k=1}^{N_r} \cup \left\{ \hat{u}(\mathbf{x}_i^k, t_i^k; \theta) \right\}_{k=1}^{N_i} \cup \left\{ \hat{u}(\mathbf{x}_b^k, t_b^k; \theta) \right\}_{k=1}^{N_b} \cup \left\{ \hat{u}(\mathbf{x}_d^k, t_d^k; \theta) \right\}_{k=1}^{N_d}$.

The training process of PINNs involves a range of hyperparameters that need to be carefully tuned, including the number of hidden layers, neurons per layer, the initialization of neural networks, the number and distribution of data points in training datasets, types of activation functions, optimizer settings, and the loss weights. Among these hyperparameters, determining the appropriate values for the loss weights is crucial, as it significantly impacts the performance of PINNs [21, 42]. This challenge is addressed by an adaptive weights algorithm [25], which will be briefly discussed in the following subsection.

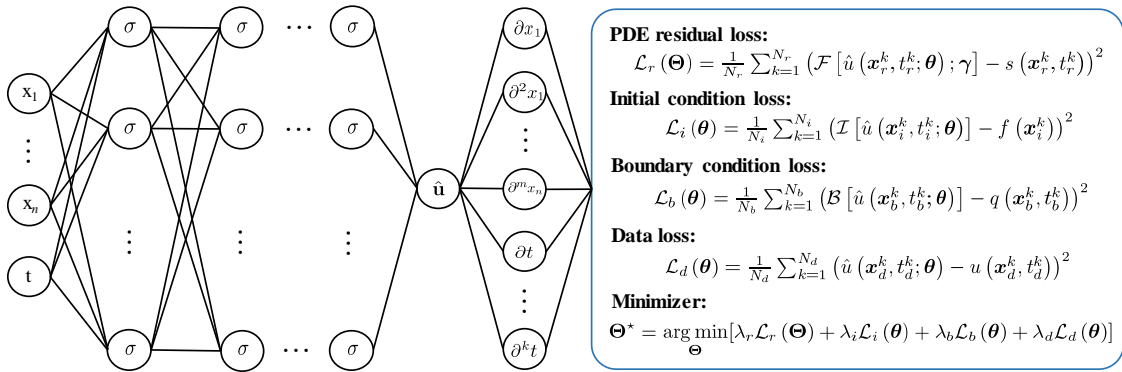


Figure 1: Schematic of PINNs for solving inverse problems in PDEs.

2.3. Adaptive weights algorithm

Consider the minimization of the loss function in Eq. (7) under the framework of a continuous-time process [25], where both Θ and loss weights are considered as functions of the training time τ . Utilizing the gradient descent method with an infinitesimally small learning rate $d\tau$ to minimize the loss function, an update rule can be expressed by [25]

$$\frac{d\Theta}{d\tau} = -\nabla \mathcal{L}(\Theta), \quad (13)$$

where ∇ is the gradient operator. By substituting $\mathcal{L}(\Theta)$ in Eq. (7) into Eq. (13), one has the NTK, denoted as \mathbf{K} , that satisfies the following expression [25]:

$$\begin{bmatrix} \frac{d\mathcal{F}[\hat{u}(\mathbf{x}_r, t_r; \boldsymbol{\theta}(\tau)); \boldsymbol{\gamma}(\tau)]}{d\tau} \\ \frac{d\mathcal{I}[\hat{u}(\mathbf{x}_i, t_i; \boldsymbol{\theta}(\tau))]}{d\tau} \\ \frac{d\mathcal{B}[\hat{u}(\mathbf{x}_b, t_b; \boldsymbol{\theta}(\tau))]}{d\tau} \\ \frac{d\hat{u}(\mathbf{x}_d, t_d; \boldsymbol{\theta}(\tau))}{d\tau} \end{bmatrix} = -\mathbf{K} \begin{bmatrix} \mathcal{F}[\hat{u}(\mathbf{x}_r, t_r; \boldsymbol{\theta}(\tau)); \boldsymbol{\gamma}(\tau)] - s(\mathbf{x}_r, t_r) \\ \mathcal{I}[\hat{u}(\mathbf{x}_i, t_i; \boldsymbol{\theta}(\tau))] - f(\mathbf{x}_i) \\ \mathcal{B}[\hat{u}(\mathbf{x}_b, t_b; \boldsymbol{\theta}(\tau))] - q(\mathbf{x}_b, t_b) \\ \hat{u}(\mathbf{x}_d, t_d; \boldsymbol{\theta}(\tau)) - u(\mathbf{x}_d, t_d) \end{bmatrix}, \quad (14)$$

where

$$\mathbf{K} = \begin{bmatrix} \frac{2\lambda_r}{N_r} \mathbf{J}_r \\ \frac{2\lambda_i}{N_i} \mathbf{J}_i \\ \frac{2\lambda_b}{N_b} \mathbf{J}_b \\ \frac{2\lambda_d}{N_d} \mathbf{J}_d \end{bmatrix} \begin{bmatrix} \mathbf{J}_r^T & \mathbf{J}_i^T & \mathbf{J}_b^T & \mathbf{J}_d^T \end{bmatrix}, \quad (15)$$

with the Jacobian matrices $\mathbf{J}_r \in \mathbb{R}^{N_r \times M}$, $\mathbf{J}_i \in \mathbb{R}^{N_i \times M}$, $\mathbf{J}_b \in \mathbb{R}^{N_b \times M}$ and $\mathbf{J}_d \in \mathbb{R}^{N_d \times M}$ of $\mathcal{F}[\hat{u}(\mathbf{x}_r, t_r; \boldsymbol{\theta}); \boldsymbol{\gamma}] \in \mathbb{R}^{N_r}$, $\mathcal{I}[\hat{u}(\mathbf{x}_i, t_i; \boldsymbol{\theta})] \in \mathbb{R}^{N_i}$, $\mathcal{B}[\hat{u}(\mathbf{x}_b, t_b; \boldsymbol{\theta})] \in \mathbb{R}^{N_b}$ and $\hat{u}(\mathbf{x}_d, t_d; \boldsymbol{\theta}) \in \mathbb{R}^{N_d}$ with respect to $\Theta \in \mathbb{R}^M$, respectively. The entries of the diagonal components of \mathbf{K} in the n -th row and m -th column are expressed by

$$\frac{2\lambda_r}{N_r} [\mathbf{J}_r \mathbf{J}_r^T]_{nm} = \frac{2\lambda_r}{N_r} \left\langle \frac{d\mathcal{F}[\hat{u}(\mathbf{x}_r^n, t_r^n; \boldsymbol{\theta}); \boldsymbol{\gamma}]}{d\Theta}, \frac{d\mathcal{F}[\hat{u}(\mathbf{x}_r^m, t_r^m; \boldsymbol{\theta}); \boldsymbol{\gamma}]}{d\Theta} \right\rangle, \quad (16)$$

$$\frac{2\lambda_i}{N_i} [\mathbf{J}_i \mathbf{J}_i^T]_{nm} = \frac{2\lambda_i}{N_i} \left\langle \frac{d\mathcal{I}[\hat{u}(\mathbf{x}_i^n, t_i^n; \boldsymbol{\theta})]}{d\boldsymbol{\theta}}, \frac{d\mathcal{I}[\hat{u}(\mathbf{x}_i^m, t_i^m; \boldsymbol{\theta})]}{d\boldsymbol{\theta}} \right\rangle, \quad (17)$$

$$\frac{2\lambda_b}{N_b} [\mathbf{J}_b \mathbf{J}_b^T]_{nm} = \frac{2\lambda_b}{N_b} \left\langle \frac{d\mathcal{B}[\hat{u}(\mathbf{x}_b^n, t_b^n; \boldsymbol{\theta})]}{d\boldsymbol{\theta}}, \frac{d\mathcal{B}[\hat{u}(\mathbf{x}_b^m, t_b^m; \boldsymbol{\theta})]}{d\boldsymbol{\theta}} \right\rangle, \quad (18)$$

and

$$\frac{2\lambda_d}{N_d} [\mathbf{J}_d \mathbf{J}_d^T]_{nm} = \frac{2\lambda_d}{N_d} \left\langle \frac{d\hat{u}(\mathbf{x}_d^n, t_d^n; \boldsymbol{\theta})}{d\boldsymbol{\theta}}, \frac{d\hat{u}(\mathbf{x}_d^m, t_d^m; \boldsymbol{\theta})}{d\boldsymbol{\theta}} \right\rangle, \quad (19)$$

where $\langle \cdot, \cdot \rangle$ represents the inner product. The convergence rates of $\mathcal{F}[\hat{u}(\mathbf{x}_r, t_r; \boldsymbol{\theta}); \boldsymbol{\gamma}]$, $\mathcal{I}[\hat{u}(\mathbf{x}_i, t_i; \boldsymbol{\theta})]$, $\mathcal{B}[\hat{u}(\mathbf{x}_b, t_b; \boldsymbol{\theta})]$ and $\hat{u}(\mathbf{x}_d, t_d; \boldsymbol{\theta})$ are proportional to $\frac{\lambda_j}{N_j} \text{tr}(\mathbf{J}_j \mathbf{J}_j^T)$ for $j = r, i, b$, and d , respectively, where $\text{tr}(\cdot)$ denotes the trace of a matrix [25].

Based on these observations, an adaptive weights algorithm was developed in Ref. [25]. The algorithm dynamically adjusts the loss weights by ensuring that $\frac{\lambda_j}{N_j} \text{tr}(\mathbf{J}_j \mathbf{J}_j^T)$ is equal for $j = r, i, b$, and d . Hence, the loss weights can be expressed by

$$\lambda_j = \frac{N_j R}{\text{tr}(\mathbf{J}_j \mathbf{J}_j^T)}, \quad j = r, i, b, \text{ and } d, \quad (20)$$

where

$$R = \frac{\text{tr}(\mathbf{J}_r \mathbf{J}_r^T)}{N_r} + \frac{\text{tr}(\mathbf{J}_i \mathbf{J}_i^T)}{N_i} + \frac{\text{tr}(\mathbf{J}_b \mathbf{J}_b^T)}{N_b} + \frac{\text{tr}(\mathbf{J}_d \mathbf{J}_d^T)}{N_d}. \quad (21)$$

To facilitate the minimization process in PINNs, a two-step training approach is often utilized [43, 44, 45]. It begins with the Adam optimizer [46], which is an advanced variation of stochastic gradient descent. Subsequently, the L-BFGS optimizer [47], a quasi-Newton method, is employed. When the adaptive weights algorithm is applied, the loss weights are updated every 1,000 iterations for the Adam optimizer [25, 48]. Besides, the loss weights are then fixed for the L-BFGS optimizer [48].

2.4. DG-PINNs for solving inverse problems

As above-mentioned, the objective of solving an inverse problem is to accurately estimate $\boldsymbol{\gamma}$ from the relevant PDE and observed data. This objective is achieved by minimizing the composite loss function in Eq. (7). It is observed that the value of

$\mathcal{L}_r(\Theta)$ depends on both of γ and θ , while the values of $\mathcal{L}_i(\theta)$, $\mathcal{L}_b(\theta)$ and $\mathcal{L}_d(\theta)$ depend only on θ . Specifically, $\mathcal{L}_r(\Theta)$ ensures that $\hat{u}(\mathbf{x}, t; \theta)$ satisfies the PDE, $\mathcal{L}_i(\theta)$ and $\mathcal{L}_b(\theta)$ ensure that $\hat{u}(\mathbf{x}, t; \theta)$ satisfies the initial and boundary conditions, respectively, and $\mathcal{L}_d(\theta)$ ensures that $\hat{u}(\mathbf{x}, t; \theta)$ fits the observed data. However, simultaneously minimizing all of these loss terms can result in a phenomenon: $\mathcal{L}_r(\Theta)$ is rapidly minimized even with an inaccurate γ , while $\mathcal{L}_d(\theta)$ remains high in the early training stages [9, 40, 14]. Moreover, the trend of $\mathcal{L}_i(\theta)$ and $\mathcal{L}_b(\theta)$ is uncertain. This phenomenon results in additional training iterations, aiming for a more accurate γ and lower $\mathcal{L}(\Theta)$. These additional iterations are computationally costly due to the computations of the derivatives in $\mathcal{L}_r(\Theta)$ and, if existing, $\mathcal{L}_i(\theta)$ and $\mathcal{L}_b(\theta)$ for each iteration.

Unlike PINNs, data-driven neural networks have the loss function only with $\mathcal{L}_d(\theta)$, which can be efficiently minimized due to the absence of derivatives in $\mathcal{L}_d(\theta)$. It can be assumed that when obtaining a minimizer θ_d for $\mathcal{L}_d(\theta)$ from a data-driven neural network, θ_d can approximate the optimal parameters θ^* for PINNs. When initialized with the minimizer θ_d , PINNs can start with a favorable initial θ , which can lead to quicker convergence and more accurate estimation of γ in the optimization process with the composite loss function in Eq. (7). Based on this logic, a novel framework, referred to as data-guided PINNs (DG-PINNs), is proposed.

The DG-PINNs consist of two phases: a pre-training phase and a fine-tuning phase. The pre-training phase is equivalent to a data-driven neural network training methodology, where the loss function only contains $\mathcal{L}_d(\theta)$. The fine-tuning phase follows the PINN methodology as described in Sec. 2.2, in which $\mathcal{L}(\Theta)$ in Eq. (7) is to be minimized. In the fine-tuning phase, the initial parameters of the neural network, denoted by θ_0 , are the minimizer θ_d obtained in the pre-training phase. When $\theta_d \approx \theta^*$, the fine-tuning phase not only facilitates accurate estimation of γ but also requires fewer iterations in the minimization of $\mathcal{L}(\Theta)$. Since the pre-training phase requires significantly lower computational costs compared to the fine-tuning phase, DG-PINNs would offer a more effective and computationally efficient approach for solving inverse problems in comparison to existing PINNs. A schematic illustration of the two-phase DG-PINNs for

solving inverse problems is shown in Fig. 2.

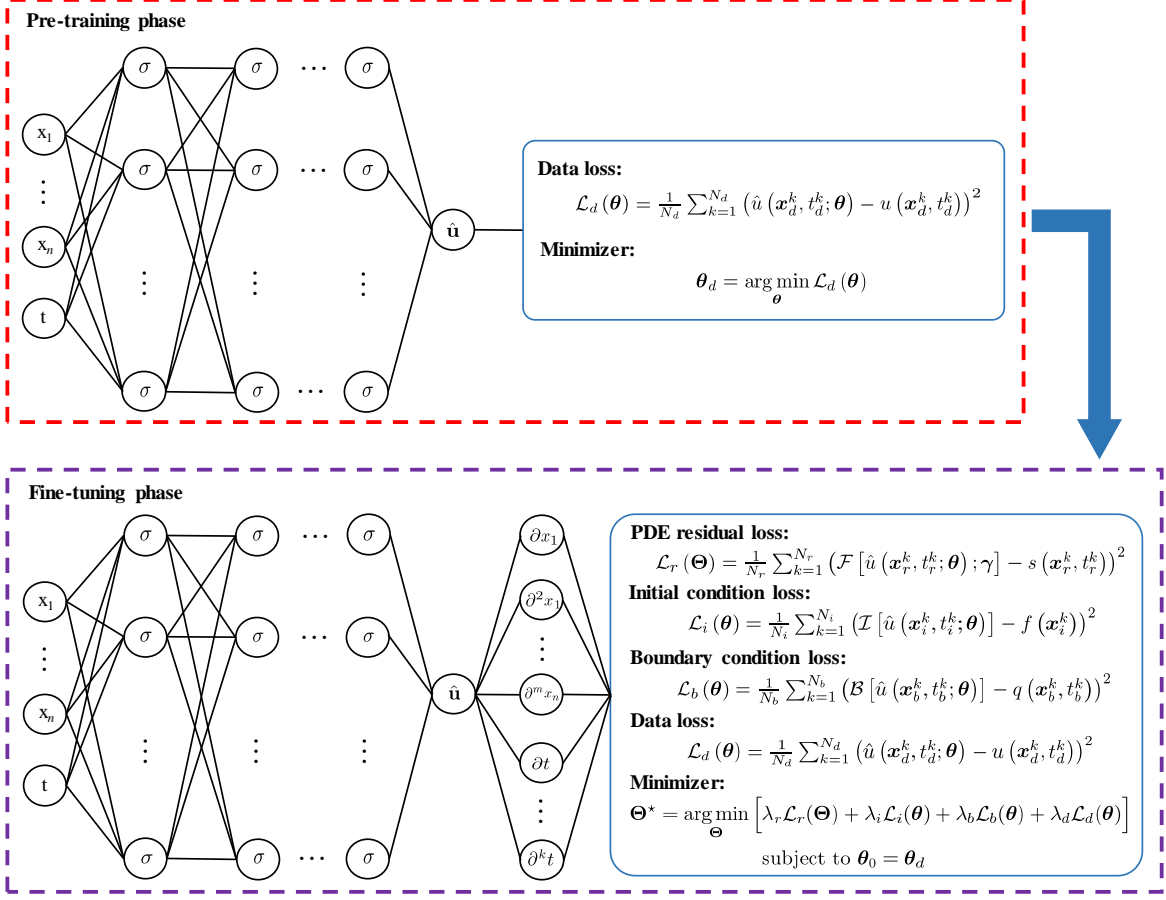


Figure 2: Schematic of DG-PINNs for solving inverse problems in PDEs with two phases: the pre-training and fine-tuning phases.

To efficiently execute the DG-PINNs, the Adam optimizer and L-BFGS optimizer are used in the pre-training and fine-tuning phases, respectively. When the pre-training phase is finished, the values of λ_r , λ_i , λ_b and λ_d will be evaluated using the adaptive weights algorithm, and they remain constant throughout the fine-tuning phase that follows. To evaluate the accuracy of the predictions of DG-PINNs at the end of the fine-tuning phase, a testing dataset $\{\mathbf{x}_t^k, t_t^k, u(\mathbf{x}_t^k, t_t^k)\}_{k=1}^{N_t}$ with the number of data points N_t is created. The relative L^2 error between $\mathbf{u}_t = \{u(\mathbf{x}_t^k, t_t^k)\}_{k=1}^{N_t}$ and the corresponding prediction $\hat{\mathbf{u}}_t = \{\hat{u}(\mathbf{x}_t^k, t_t^k; \theta)\}_{k=1}^{N_t}$ from DG-PINNs is utilized as a metric, which is defined as

$$\mathcal{R}_t = \frac{\|\mathbf{u}_t - \hat{\mathbf{u}}_t\|_2}{\|\mathbf{u}_t\|_2}, \quad (22)$$

where $\|\cdot\|_2$ denotes the L^2 norm.

The pseudo-code for the DG-PINNs is described in Algorithm 1.

Algorithm 1 DG-PINNs.

Input: Training datasets and hyperparameters

Output: Optimal parameters $\boldsymbol{\theta}^*$ and estimated unknown parameters $\boldsymbol{\gamma}^*$: $\Theta^* = \{\boldsymbol{\theta}^*, \boldsymbol{\gamma}^*\}$

Pre-training phase

- 1: Initialize neural network parameters $\boldsymbol{\theta}$
- 2: Set the maximum number of iterations M_1
- 3: **for** *iteration* from 1 to M_1 **do**
- 4: Calculate the data loss $\mathcal{L}_d(\boldsymbol{\theta})$ using Eq. (11)
- 5: Update $\boldsymbol{\theta}$ using the Adam optimizer
- 6: **end for**

Fine-tuning phase

- 7: Initialize unknown parameters $\boldsymbol{\gamma}$
 - 8: Estimate loss weights $\lambda_r, \lambda_i, \lambda_b$ and λ_d
 - 9: Set the maximum number of iterations M_2
 - 10: **for** *iteration* from 1 to M_2 **do**
 - 11: Calculate the composite loss function $\mathcal{L}(\Theta)$ using Eq. (7)
 - 12: Update Θ using the L-BFGS optimizer
 - 13: **end for**
 - 14: Set $\Theta^* = \Theta$
 - 15: **return** Θ^*
-

3. Numerical Investigations

In this section, a series of numerical investigations are conducted to validate the effectiveness, noise-robustness, and efficiency of the DG-PINNs in solving inverse problems related to various PDEs, including the heat equation, wave equation, Euler–Bernoulli beam equation and Navier–Stokes equation. Throughout these numerical investigations, three-layer fully-connected networks are used, where each hidden layer has 100 neurons. The activation function is the hyperbolic tangent activation function. In this work, the initialization of neural networks is achieved using a uniform distribution in Ref. [49]. The initialization of unknown parameters within PDEs is achieved using a uniform distribution in the interval $[0, 1)$.

In the numerical investigations for each inverse problem, sensitivity analyses of the DG-PINNs results are conducted to examine the effects of the maximum number of iterations M_1 in the pre-training phase and the number of data points in training datasets for the data loss. The noise-robustness of the DG-PINNs is evaluated by introducing varying levels of white Gaussian noise to observed data. Besides, a comparative analysis between DG-PINNs and PINNs is performed for each inverse problem.

3.1. One-dimensional heat equation

The one-dimensional heat equation is a PDE that models the temporal distribution of heat within a given region. It is a fundamental equation in the field of heat transfer and is expressed in the dimensionless spatial-temporal domain $(x, t) \in [0, 1] \times [0, 1]$ by

$$\frac{\partial u(x, t)}{\partial t} - \beta^2 \frac{\partial^2 u(x, t)}{\partial x^2} = 0, \quad (x, t) \in [0, 1] \times [0, 1], \quad (23)$$

where β^2 denotes the thermal diffusivity of the material. This equation is subject to the following initial condition:

$$u(x, 0) = \sin(10\pi x), \quad x \in [0, 1], \quad (24)$$

and boundary conditions:

$$u(0, t) = u(1, t) = 0, \quad t \in [0, 1]. \quad (25)$$

Applying the method of separation of variables [50], the solution $u(x, t)$ is expressed by

$$u(x, t) = \exp(-(10\pi\beta)^2 t) \sin(10\pi x). \quad (26)$$

Observed data for $\beta = \frac{1}{20}$ are acquired on a 201×201 grid evenly distributed within the spatial-temporal domain. The grid uses increments of 0.005 for both spatial and temporal dimensions. From the observed data, training datasets $\{x_d^k, t_d^k, u(x_d^k, t_d^k)\}_{k=1}^{N_d}$ with $N_d = 10,000$ and $\{x_r^k, t_r^k, 0\}_{k=1}^{N_r}$ with $N_r = 2,000$ are randomly sampled in the grid, i.e., $(x, t) \in [0, 1] \times [0, 1]$, $\{x_i^k, 0, u(x_i^k, 0)\}_{k=1}^{N_i}$ with $N_i = 100$ and $\{x_b^k, t_b^k, 0\}_{k=1}^{N_b}$ with

$N_b = 200$ are randomly sampled in the initial snapshot, i.e., $t = 0$ with $x \in [0, 1]$, and boundaries i.e., $x = 0$ or 1 with $t \in [0, 1]$, respectively. Finally, the remaining, unsampled observed data are grouped as a testing dataset $\{x_t^k, t_t^k, u(x_t^k, t_t^k)\}_{k=1}^{N_t}$. These training and testing datasets are used for all investigations in the heat equation by default. For the heat equation in Eq. (23), the PDE residual loss is expressed by

$$\mathcal{L}_r(\Theta) = \frac{1}{N_r} \sum_{k=1}^{N_r} \left(\frac{\partial \hat{u}(x_r^k, t_r^k; \Theta)}{\partial t} - \tilde{\beta}^2 \frac{\partial^2 \hat{u}(x_r^k, t_r^k; \Theta)}{\partial x^2} \right)^2, \quad (27)$$

where $\tilde{\beta}$ is the unknown parameter to be estimated.

To conduct a sensitivity analysis on the maximum number of iterations M_1 in the pre-training phase, fifteen DG-PINN models with $M_1 = \{2,000, 3,000, 4,000, 5,000, 6,000, 7,000, 8,000, 9,000, 10,000, 15,000, 20,000, 25,000, 30,000, 40,000, 50,000\}$, are trained. In this sensitivity analysis, the Adam optimizer has a learning rate of 0.001, and the L-BFGS optimizer has a learning rate of 0.1 with the maximum number of iterations $M_2 = 10,000$. The optimizer settings are maintained consistently for the sensitivity analysis on M_1 across the other PDEs. The accuracy of the predictions from the fifteen DG-PINN models is evaluated by \mathcal{R}_t as shown in Fig. 3(a). It can be seen that the values of \mathcal{R}_t remain below 6×10^{-3} for all M_1 . Besides, the absolute percentage error (APE) between $\tilde{\beta}^2$ and β^2 for each DG-PINN model is shown in Fig. 3(b). The maximum APE value is 4.77% with $M_1 = 2000$; however a definite correlation between the APE value and M_1 cannot be observed. Further, since all the obtained APE values associated with the wide range of M_1 values are considered low, DG-PINNs can solve the inverse problem with an accurate estimation of β^2 , which highlights the robustness of the selection of M_1 for DG-PINNs.

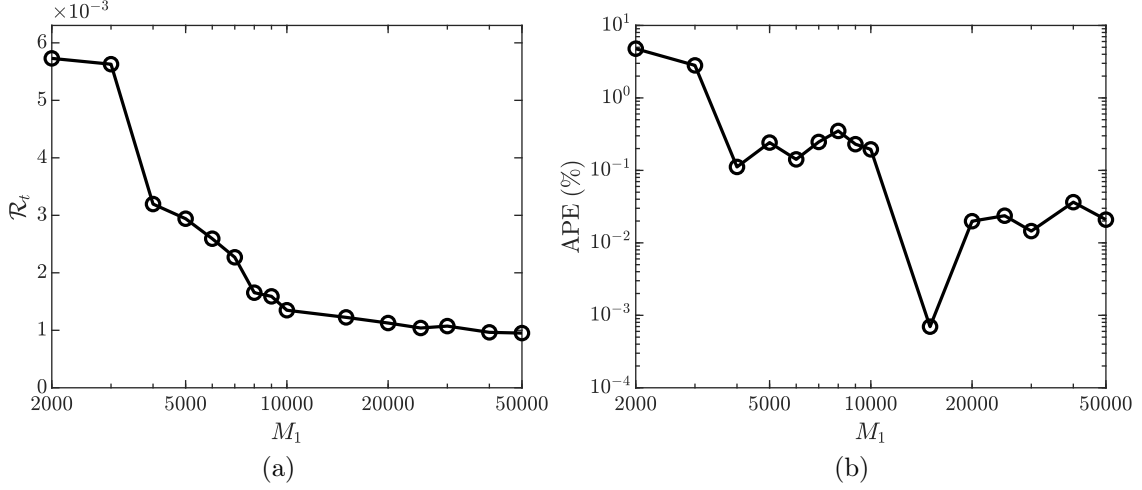


Figure 3: Sensitivity analysis on M_1 for the heat equation: (a) the relative L^2 errors between the testing data and the corresponding prediction from DG-PINN models, and (b) the absolute percentage error (APE) between $\tilde{\beta}^2$ and β^2 .

To conduct a sensitivity analysis on N_d , fifteen DG-PINN models with $\{x_d^k, t_d^k, u(x_d^k, t_d^k)\}_{k=1}^{N_d}$ with $N_d = \{500, 600, 700, 800, 900, 1,000, 2,000, 3,000, 4,000, 5,000, 6,000, 7,000, 8,000, 9,000, 10,000\}$ are trained. The Adam optimizer has a learning rate of 0.001 with maximum number of iterations $M_1 = 20,000$, and the L-BFGS optimizer has a learning rate of 0.1 with the maximum number of iterations $M_2 = 10,000$. The optimizer settings are maintained consistently for the sensitivity analysis on N_d across the other PDEs. The accuracy of the predictions from the fifteen DG-PINN models is evaluated by \mathcal{R}_t shown in Fig. 4(a). It can be seen that the values of \mathcal{R}_t remain below 4×10^{-3} for all N_d values. Besides, the APE between $\tilde{\beta}^2$ and β^2 for each DG-PINN model is shown in Fig. 4(b). While the maximum APE value is 0.18% with $N_d = 5,000$, no clear correlation between the APE value and N_d cannot be observed. Further, since all the obtained APE values associated with the wide range of N_d values are considered low, DG-PINNs can solve the inverse problem with an accurate estimation of β^2 , which highlights the robustness of the selection of N_d for DG-PINNs.

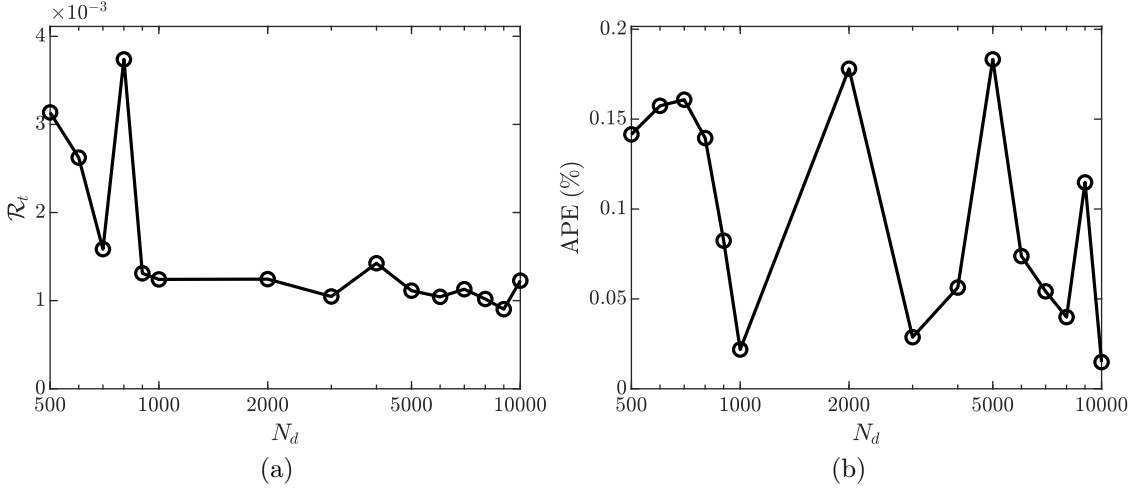


Figure 4: Sensitivity analysis on N_d for the heat equation: (a) the relative L^2 errors between the testing data and the corresponding prediction from DG-PINN models, and (b) the absolute percentage error (APE) between $\tilde{\beta}^2$ and β^2 .

To investigate the noise-robustness of DG-PINNs, four DG-PINN models are trained using observed data contaminated with white Gaussian noise at signal-to-noise ratios (SNRs) of 40, 35, 30, and 25 dB, respectively. Training datasets are sampled from these noise-contaminated observed data with the same scheme as that implemented in the sensitivity analysis on M_1 for the heat equation. The Adam optimizer has a learning rate of 0.001 with $M_1 = 50,000$, whereas the L-BFGS optimizer has a learning rate of 0.1 with $M_2 = 20,000$. The optimizer settings are maintained consistently for the noise-robustness analysis across the other PDEs. The accuracy of the predictions from the four DG-PINN models is evaluated by \mathcal{R}_t , which is calculated as 1.47×10^{-3} , 2.25×10^{-3} , 4.47×10^{-3} , and 9.67×10^{-3} in the case of SNR = 40, 35, 30, and 25 dB, respectively. Besides, the APE between $\tilde{\beta}^2$ and β^2 for each DG-PINN model is calculated as 0.16%, 0.14%, 0.24%, and 0.63% in the case of SNR = 40, 35, 30, and 25 dB, respectively. These results indicate that DG-PINNs are capable of accurately solving the inverse problem of the heat equation in the presence of noise contamination.

To compare the efficiency of DG-PINNs and PINNs, ten independent trials are conducted for both DG-PINNs and PINNs to solve the inverse problem of the heat equation. In terms of optimizer settings, the Adam optimizer has a learning rate of 0.001 with

$M_1 = 20,000$, whereas the L-BFGS optimizer has a learning rate of 0.1 with $M_2 = 10,000$. The adaptive weights algorithm, outlined in Section 2.3, is utilized to adjust loss weights every 1,000 iterations in PINNs for the Adam optimizer. The optimizer settings are maintained consistently for the comparative analysis between DG-PINNs and PINNs across the other PDEs. In one of the ten PINN trials, $\mathcal{L}(\Theta)$ does not converge. The trial is considered an outlier and excluded in the discussion that follows. With other convergent PINNs and DG-PINNs, the averaged \mathcal{R}_t , APE between $\tilde{\beta}^2$ and β^2 , and training time are listed in Table 1. It is shown that \mathcal{R}_t and APE of both PINN and DG-PINNs are small, indicating that they both provide similarly accurate predictions. Though the DG-PINNs have higher \mathcal{R}_t and APE values than PINN, the training time for DG-PINNs is significantly shorter than that for PINNs. These results demonstrate that DG-PINNs are six times faster than PINNs in solving the inverse problem of the heat equation, achieving comparable accuracy in both predictions and the estimation of β^2 .

Table 1: Results of the comparative analysis between DG-PINNs and PINNs for the heat equation.

Method	\mathcal{R}_t	APE	Training time
PINN	1.05×10^{-3}	0.05%	26.83 min
DG-PINN	1.44×10^{-3}	0.14%	4.26 min

3.2. One-dimensional wave equation

The propagation of a wave through a one-dimensional medium is a fundamental phenomenon observed in various physical systems. This process is governed by the one-dimensional wave equation, a crucial mathematical model in the field of wave propagation. Formally, within the dimensionless spatial-temporal domain $(x, t) \in [0, 1] \times [0, 1]$, the equation is expressed by

$$\frac{\partial^2 u(x, t)}{\partial t^2} - c^2 \frac{\partial^2 u(x, t)}{\partial x^2} = 0, \quad (x, t) \in [0, 1] \times [0, 1], \quad (28)$$

where c denotes the wave speed. This equation is subject to initial conditions:

$$\begin{cases} u(x, 0) = \sin(\pi x) + \frac{1}{2} \sin(4\pi x) \\ \frac{\partial u(x, 0)}{\partial t} = 0 \end{cases}, \quad x \in [0, 1], \quad (29)$$

and boundary conditions:

$$u(0, t) = u(1, t) = 0, \quad t \in [0, 1]. \quad (30)$$

By applying the method of separation of variables [50], the solution $u(x, t)$ can be analytically expressed by

$$u(x, t) = \sin(\pi x) \cos(c\pi t) + \frac{1}{2} \sin(4\pi x) \cos(4c\pi t). \quad (31)$$

Observed data of the wave equation with $c = 2$ are acquired on a 201×201 grid uniformly distributed within the domain $(x, t) \in [0, 1] \times [0, 1]$. The acquisition process for the training and testing datasets is the same as that implemented in the sensitivity analysis on M_1 for the heat equation in Sec. 3.1. These training and testing datasets are used for all investigations in the wave equation by default. The PDE residual loss $\mathcal{L}_r(\Theta)$ for solving the inverse problem in the wave equation is expressed by

$$\mathcal{L}_r(\Theta) = \frac{1}{N_r} \sum_{k=1}^{N_r} \left(\frac{\partial^2 \hat{u}(x_r^k, t_r^k; \Theta)}{\partial t^2} - \tilde{c}^2 \frac{\partial^2 \hat{u}(x_r^k, t_r^k; \Theta)}{\partial x^2} \right)^2, \quad (32)$$

where \tilde{c} is the unknown parameter to be estimated. Two initial condition losses $\mathcal{L}_{i1}(\Theta)$ and $\mathcal{L}_{i2}(\Theta)$ are defined, which are expressed by

$$\mathcal{L}_{i1}(\Theta) = \frac{1}{N_i} \sum_{k=1}^{N_i} \left(\hat{u}(x_i^k, 0; \Theta) - \sin(\pi x_i^k) - \frac{1}{2} \sin(4\pi x_i^k) \right)^2, \quad (33)$$

and

$$\mathcal{L}_{i2}(\Theta) = \frac{1}{N_i} \sum_{k=1}^{N_i} \left(\frac{\partial \hat{u}(x_i^k, 0; \Theta)}{\partial t} \right)^2, \quad (34)$$

respectively. Boundary condition loss $\mathcal{L}_b(\Theta)$ and the data loss $\mathcal{L}_d(\Theta)$ can be calculated using Eqs. (10) and (11), respectively. The composite loss function for the wave equation

can be expressed by

$$\mathcal{L}(\Theta) = \lambda_r \mathcal{L}_r(\Theta) + \lambda_{i1} \mathcal{L}_{i1}(\theta) + \lambda_{i2} \mathcal{L}_{i2}(\theta) + \lambda_b \mathcal{L}_b(\theta) + \lambda_d \mathcal{L}_d(\theta). \quad (35)$$

To conduct a sensitivity analysis on M_1 for the wave equation, fifteen DG-PINN models are trained with same M_1 values as those specified in the sensitivity analysis on M_1 for the heat equation in Sec. 3.1. The accuracy of the predictions from the fifteen DG-PINN models is evaluated by \mathcal{R}_t shown in Fig. 5(a). It can be seen that the values of \mathcal{R}_t remain below 3×10^{-3} for all M_1 . Besides, the APE between \tilde{c}^2 and c^2 for each DG-PINN model is shown in Fig. 5(b). The maximum APE value is 0.027% with $M_1 = 2,000$; however, no indicative correlation between the APE value and M_1 can be observed. Further, since all the obtained APE values associated with the wide range of M_1 values are considered low, DG-PINNs can solve the inverse problem with an accurate estimation of c^2 , which highlights the robustness of the selection of M_1 for DG-PINNs.

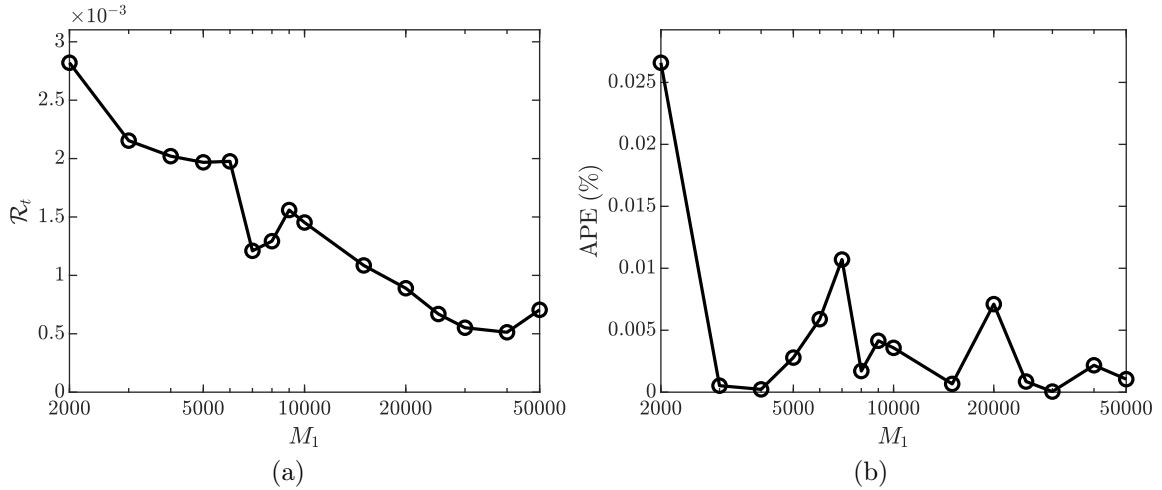


Figure 5: Sensitivity analysis on M_1 for the wave equation: (a) the relative L^2 errors between the testing data and the corresponding predictions from the DG-PINN models, and (b) the absolute percentage error (APE) between \tilde{c}^2 and c^2 .

To conduct a sensitivity analysis on N_d , fifteen DG-PINN models are trained using $\{x_d^k, t_d^k, u(x_d^k, t_d^k)\}_{k=1}^{N_d}$ for $\mathcal{L}_d(\theta)$ in the wave equation, with N_d values matching those used in the sensitivity analysis for the heat equation. The accuracy of the predictions from the fifteen DG-PINN models is evaluated by \mathcal{R}_t shown in Fig. 6(a). It can be seen that

the values of \mathcal{R}_t remain below 1.1×10^{-3} . Besides, the APE between \tilde{c}^2 and c^2 for each DG-PINN model is shown in Fig. 6(b). While the maximum APE value is 0.009% with $N_d = 800$, an indicative correlation between the APE value and N_d cannot be observed. Further, since all the obtained APE values associated with the wide range of N_d values are considered low, DG-PINNs can solve the inverse problem with an accurate estimation of c^2 , which highlights the robustness of the selection of N_d for DG-PINNs.

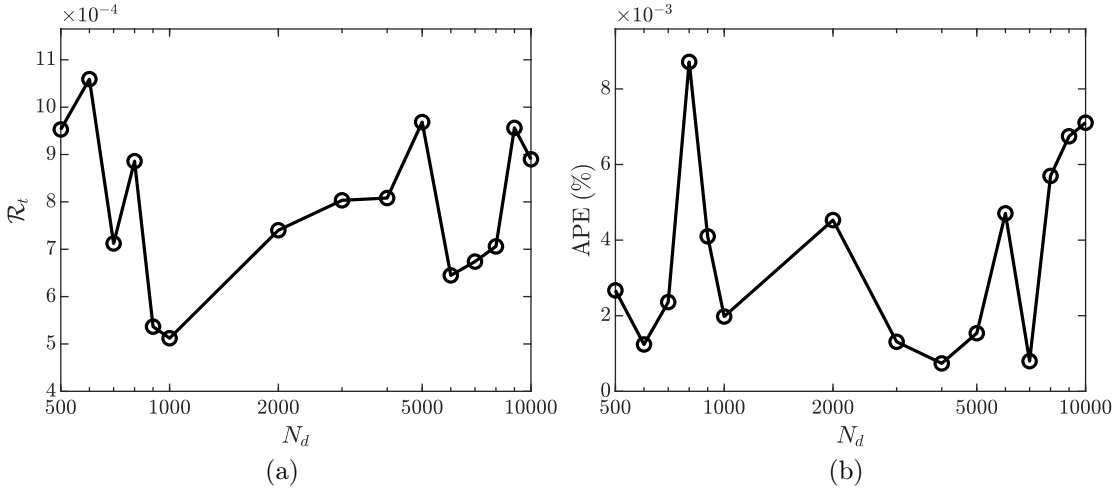


Figure 6: Sensitivity analysis on N_d for the wave equation: (a) the relative L^2 errors between the testing data and the corresponding predictions of the DG-PINN models, and (b) the absolute percentage error (APE) between \tilde{c}^2 and c^2 .

To investigate the noise-robustness of DG-PINNs for the wave equation, four DG-PINN models are trained using observed data contaminated with white Gaussian noise at SNRs of 40, 35, 30, and 25 dB, respectively. Training datasets are sampled from these noise-contaminated observed data. The accuracy of the predictions from the four DG-PINN models is evaluated using \mathcal{R}_t , which is calculated as 6.59×10^{-4} , 1.16×10^{-3} , 2.00×10^{-3} , and 3.63×10^{-3} for SNRs of 40, 35, 30, and 25 dB, respectively. Besides, the APE between \tilde{c}^2 and c^2 for each DG-PINN model is calculated as 0.002%, 0.003%, 0.007%, and 0.006% in the case of SNR = 40, 35, 30, and 25 dB, respectively. These results indicate that DG-PINNs are capable of accurately solving the inverse problem of the wave equation in the presence of noise contamination.

To evaluate the efficiency of PINNs and DG-PINNs, both approaches are applied in ten independent trials to solve the inverse problem of the wave equation. The averaged

\mathcal{R}_t , APE between \tilde{c}^2 and c^2 , and training time are listed in Table 2. It is shown that \mathcal{R}_t for DG-PINNs is lower than that for PINNs, indicating that DG-PINNs provide more accurate predictions compared to PINNs. Regarding the APE between \tilde{c}^2 and c^2 , both DG-PINNs and PINNs exhibit high accuracy with significantly small APE values. Besides, the computational efficiency of DG-PINNs is significantly higher, as evidenced by markedly reduced training times compared to PINNs. These results demonstrate that DG-PINNs are six times faster than PINNs in solving the inverse problem of the wave equation, achieving comparable accuracy in both predictions and the estimation of c^2 .

Table 2: Results of the comparative analysis between DG-PINNs and PINNs for the wave equation.

Method	\mathcal{R}_t	APE	Training time
PINN	1.3×10^{-3}	0.003%	28.57 min
DG-PINN	7.49×10^{-4}	0.003%	4.57 min

3.3. Euler–Bernoulli beam equation

The Euler-Bernoulli beam equation, a fundamental principle in the field of structural analysis and engineering, describes the flexural motion of beam [51]. When considering a homogeneous beam undergoing undamped free flexural vibration, the governing equation for its flexural motion within the dimensionless spatial-temporal domain $(x, t) \in [0, 1] \times [0, 1]$ is expressed by

$$\frac{\partial^2 u(x, t)}{\partial t^2} + \alpha^2 \frac{\partial^4 u(x, t)}{\partial x^4} = 0, \quad (x, t) \in [0, 1] \times [0, 1], \quad (36)$$

where α is a parameter related to the material property of the beam. This equation is subject to initial conditions:

$$\begin{cases} u(x, 0) = \sin(\pi x) \\ \frac{\partial u(x, 0)}{\partial t} = 0 \end{cases}, \quad x \in [0, 1], \quad (37)$$

and boundary conditions:

$$\begin{cases} u(0, t) = u(1, t) = 0 \\ \frac{\partial^2 u(0, t)}{\partial x^2} = \frac{\partial^2 u(1, t)}{\partial x^2} = 0 \end{cases}, \quad t \in [0, 1]. \quad (38)$$

By applying the method of separation of variables [50], the solution $u(x, t)$ can be analytically expressed by

$$u(x, t) = \sin(\pi x) \cos(\alpha \pi^2 t). \quad (39)$$

Observed data for the beam equation with $\alpha = 1$ are acquired on a 201×201 grid uniformly distributed within the domain $(x, t) \in [0, 1] \times [0, 1]$. The acquisition of datasets for training and testing is the same as the approach implemented in the sensitivity analysis on M_1 for the heat equation in Sec. 3.1. These training and testing datasets are used for all investigations in the beam equation by default. The PDE residual loss $\mathcal{L}_r(\boldsymbol{\Theta})$ for the beam equation is expressed by

$$\mathcal{L}_r(\boldsymbol{\Theta}) = \frac{1}{N_r} \sum_{k=1}^{N_r} \left(\frac{\partial^2 \hat{u}(x_r^k, t_r^k; \boldsymbol{\theta})}{\partial t^2} + \tilde{\alpha}^2 \frac{\partial^4 \hat{u}(x_r^k, t_r^k; \boldsymbol{\theta})}{\partial x^4} \right)^2, \quad (40)$$

where $\tilde{\alpha}$ is the unknown parameter to be estimated. Two initial condition losses $\mathcal{L}_{i1}(\boldsymbol{\theta})$ and $\mathcal{L}_{i2}(\boldsymbol{\theta})$ are defined, which are expressed by

$$\mathcal{L}_{i1}(\boldsymbol{\theta}) = \frac{1}{N_i} \sum_{k=1}^{N_i} (\hat{u}(x_i^k, 0; \boldsymbol{\theta}) - \sin(\pi x_i^k))^2, \quad (41)$$

and

$$\mathcal{L}_{i2}(\boldsymbol{\theta}) = \frac{1}{N_i} \sum_{k=1}^{N_i} \left(\frac{\partial \hat{u}(x_i^k, 0; \boldsymbol{\theta})}{\partial t} \right)^2, \quad (42)$$

respectively. Two boundary condition losses $\mathcal{L}_{b1}(\boldsymbol{\theta})$ and $\mathcal{L}_{b2}(\boldsymbol{\theta})$ are defined, which are expressed by

$$\mathcal{L}_{b1}(\boldsymbol{\theta}) = \frac{1}{N_b} \sum_{k=1}^{N_b} (\hat{u}(x_b^k, t_b^k; \boldsymbol{\theta}))^2, \quad (43)$$

and

$$\mathcal{L}_{b2}(\boldsymbol{\theta}) = \frac{1}{N_b} \sum_{k=1}^{N_b} \left(\frac{\partial^2 \hat{u}(x_b^k, t_b^k; \boldsymbol{\theta})}{\partial x^2} \right)^2. \quad (44)$$

The data loss $\mathcal{L}_d(\boldsymbol{\theta})$ can be calculated using Eq. (11). The composite loss function for the beam equation can be expressed by

$$\mathcal{L}(\boldsymbol{\Theta}) = \lambda_r \mathcal{L}_r(\boldsymbol{\Theta}) + \lambda_{i1} \mathcal{L}_{i1}(\boldsymbol{\theta}) + \lambda_{i2} \mathcal{L}_{i2}(\boldsymbol{\theta}) + \lambda_{b1} \mathcal{L}_{b1}(\boldsymbol{\theta}) + \lambda_{b2} \mathcal{L}_{b2}(\boldsymbol{\theta}) + \lambda_d \mathcal{L}_d(\boldsymbol{\theta}). \quad (45)$$

To conduct a sensitivity analysis on M_1 for the beam equation, fifteen DG-PINN models are trained with same M_1 values as those specified in the sensitivity analysis on M_1 for the heat equation in Sec. 3.1. The accuracy of the predictions from the fifteen DG-PINN models is evaluated by \mathcal{R}_t shown in Fig. 7(a). It can be seen that the values of \mathcal{R}_t remain below 3×10^{-4} for all M_1 . Besides, the APE between $\tilde{\alpha}^2$ and α^2 for each DG-PINN model is shown in Fig. 7(b). The maximum APE value is 0.034% with $M_1 = 10,000$; however, no indicative correlation between the APE value and M_1 can be observed. Further, since all the obtained APE values associated with the wide range of M_1 values are considered low, DG-PINNs can solve the inverse problem with an accurate estimation of α^2 , which highlights the robustness of the selection of M_1 for DG-PINNs.

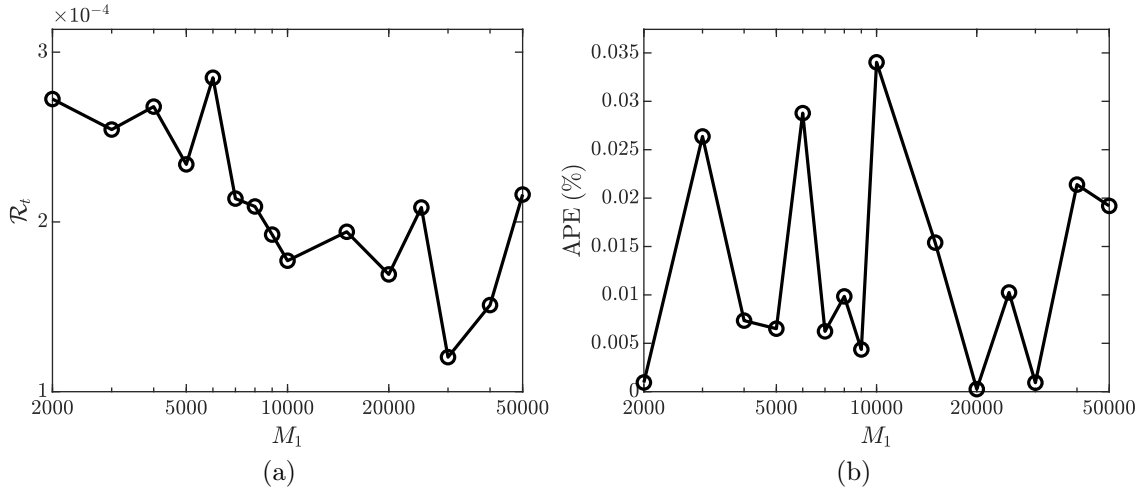


Figure 7: Sensitivity analysis on M_1 for the beam equation: (a) the relative L^2 errors between the testing data and the corresponding prediction of the DG-PINN models, and (b) the absolute percentage error (APE) between $\tilde{\alpha}^2$ and α^2 .

To conduct a sensitivity analysis on N_d , fifteen DG-PINN models are trained using $\{x_d^k, t_d^k, u(x_d^k, t_d^k)\}_{k=1}^{N_d}$ for $\mathcal{L}_d(\boldsymbol{\theta})$ in the beam equation, with N_d values matching those used in the sensitivity analysis for the heat equation. The accuracy of the predictions from the fifteen DG-PINN models is evaluated by \mathcal{R}_t shown in Fig. 8(a). It can be seen that the values of \mathcal{R}_t remain below 3×10^{-4} . Besides, the APE between $\tilde{\alpha}^2$ and α^2 for each DG-PINN model is shown in Fig. 8(b). The maximum APE value is 0.043% with $N_d = 1,000$; however, an indicative correlation between the APE value and N_d cannot be observed. Further, since all the obtained APE values associated with the wide range of N_d values are considered low, DG-PINNs can solve the inverse problem with an accurate estimation of α^2 , which highlights the robustness of the selection of N_d for DG-PINNs.

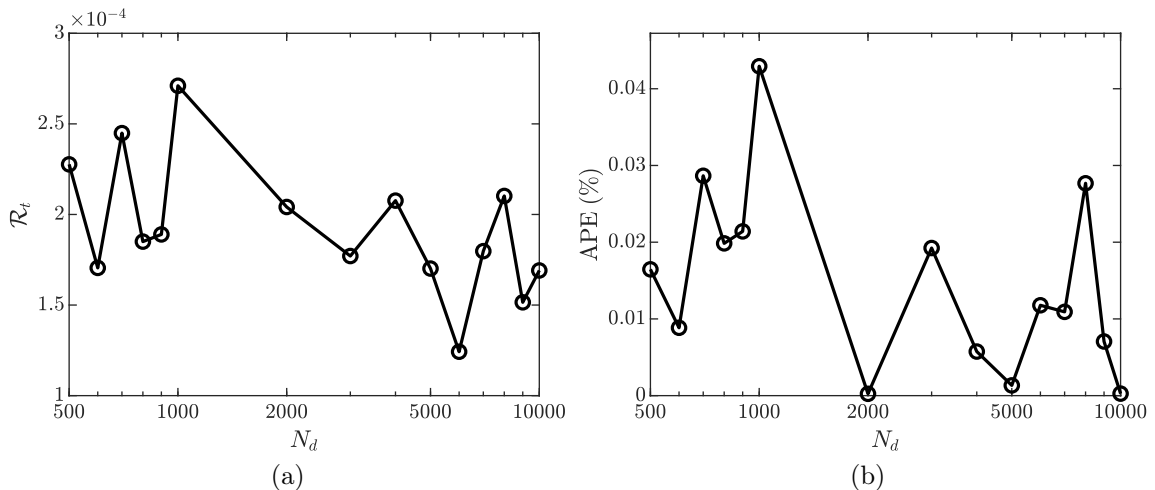


Figure 8: Sensitivity analysis of N_d for the beam equation: (a) the relative L^2 errors between the testing data and the corresponding prediction of the DG-PINN models, and (b) the absolute percentage error (APE) between $\tilde{\alpha}^2$ and α^2 .

To investigate the noise-robustness of DG-PINNs for the beam equation, four DG-PINN models are trained using observed data contaminated with white Gaussian noise at SNRs of 40, 35, 30, and 25 dB, respectively. Training datasets are sampled from these noise-contaminated observed data. The accuracy of the predictions from the four DG-PINN models is evaluated using \mathcal{R}_t , which is calculated as 4.89×10^{-4} , 8.40×10^{-4} , 1.50×10^{-3} and 3.49×10^{-3} for SNRs of 40, 35, 30, and 25 dB, respectively. Besides, the APE between $\tilde{\alpha}^2$ and α^2 for each DG-PINN model is calculated as 0.056%, 0.065%, 0.109%, and 0.852% in the case of SNR = 40, 35, 30, and 25 dB, respectively. These results indicate that DG-PINNs are capable of accurately solving the inverse problem of

the beam equation in the presence of noise contamination.

To evaluate the efficiency of PINNs and DG-PINNs, both approaches are applied in ten independent trials to solve the inverse problem of the beam equation. The averaged \mathcal{R}_t , APE between $\tilde{\alpha}^2$ versus α^2 , and training time are listed in Table 3. It is shown that \mathcal{R}_t for DG-PINNs is lower than that for PINNs, indicating that DG-PINNs provide more accurate predictions compared to PINNs. Regarding the APE between $\tilde{\alpha}^2$ and α^2 , both DG-PINNs and PINNs exhibit high accuracy with small APE values, but PINNs provide a more accurate estimation of α^2 . Besides, the training time for DG-PINNs is significantly shorter than for PINNs. These results demonstrate that DG-PINNs are six times faster than PINNs in solving the inverse problem of the beam equation, achieving comparable accuracy in both predictions and the estimation of α^2 .

Table 3: Results of the comparative analysis between DG-PINNs and PINNs for the beam equation.

Method	\mathcal{R}_t	APE	Training time
PINN	4.10×10^{-4}	0.01%	38.04 min
DG-PINN	2.62×10^{-4}	0.10%	6.43 min

3.4. Navier–Stokes equation

The Navier–Stokes equations for an incompressible fluid describe the motion of fluid substances, such as liquids and gases. These equations are fundamental in the field of fluid dynamics. For an incompressible fluid, the Navier–Stokes equations in two dimensions can be expressed by

$$\begin{cases} \frac{\partial u}{\partial t} + \beta_1 \left(u \frac{\partial u}{\partial x} + v \frac{\partial u}{\partial y} \right) = -\frac{\partial p}{\partial x} + \beta_2 \left(\frac{\partial^2 u}{\partial x^2} + \frac{\partial^2 u}{\partial y^2} \right) \\ \frac{\partial v}{\partial t} + \beta_1 \left(u \frac{\partial v}{\partial x} + v \frac{\partial v}{\partial y} \right) = -\frac{\partial p}{\partial y} + \beta_2 \left(\frac{\partial^2 v}{\partial x^2} + \frac{\partial^2 v}{\partial y^2} \right), \\ \frac{\partial u}{\partial x} + \frac{\partial v}{\partial y} = 0 \end{cases}, \quad (46)$$

where $u(x, y, t)$ and $v(x, y, t)$ denote the x - and y -component of the velocity field, respectively, and $p(x, y, t)$ denotes the pressure field.

The prototype problem of incompressible flow past a circular cylinder same as one in Ref. [2] is used, where $\beta_1 = 1$ and $\beta_2 = 0.01$. In solving the inverse problem of the Navier–Stokes equation, estimating parameter β_1 and β_2 as well as the pressure $p(x, y, t)$ are interested. A high-resolution dataset in domain $(x, y, t) \in [1, 8] \times [-2, 2] \times [0, 7]$. Training datasets $\{x_d^k, y_d^k, t_d^k, u(x_d^k, y_d^k, t_d^k), v(x_d^k, y_d^k, t_d^k)\}_{k=1}^{N_d}$ with $N_d = 10,000$ and $\{x_r^k, y_r^k, t_r^k, 0\}_{k=1}^{N_r}$ with $N_r = 2,000$ are randomly sampled in the interior of the grid. Other unused observed data are served as a testing dataset $\{x_t^k, y_t^k, t_t^k, u(x_t^k, y_t^k, t_t^k), v(x_t^k, y_t^k, t_t^k)\}_{k=1}^{N_t}$.

Assume outputs of a neural network $\hat{u}(x, y, t; \boldsymbol{\theta})$, $\hat{v}(x, y, t; \boldsymbol{\theta})$ and $\hat{p}(x, y, t; \boldsymbol{\theta})$ approximate $u(x, y, t)$, $v(x, y, t)$ and $p(x, y, t)$. The residuals $f(x, y, t; \boldsymbol{\theta})$, $g(x, y, t; \boldsymbol{\theta})$, and $h(x, y, t; \boldsymbol{\theta})$ can be given by

$$\begin{cases} f(x, y, t; \boldsymbol{\theta}) = \frac{\partial \hat{u}}{\partial t} + \tilde{\beta}_1 \left(\hat{u} \frac{\partial \hat{u}}{\partial x} + \hat{v} \frac{\partial \hat{u}}{\partial y} \right) + \frac{\partial \hat{p}}{\partial x} - \tilde{\beta}_2 \left(\frac{\partial^2 \hat{u}}{\partial x^2} + \frac{\partial^2 \hat{u}}{\partial y^2} \right) \\ g(x, y, t; \boldsymbol{\theta}) = \frac{\partial \hat{v}}{\partial t} + \tilde{\beta}_1 \left(\hat{u} \frac{\partial \hat{v}}{\partial x} + \hat{v} \frac{\partial \hat{v}}{\partial y} \right) + \frac{\partial \hat{p}}{\partial y} - \tilde{\beta}_2 \left(\frac{\partial^2 \hat{v}}{\partial x^2} + \frac{\partial^2 \hat{v}}{\partial y^2} \right), \\ h(x, y, t; \boldsymbol{\theta}) = \frac{\partial \hat{u}(x_r^k, y_r^k, t_r^k)}{\partial x} + \frac{\partial \hat{v}(x_r^k, y_r^k, t_r^k)}{\partial y} \end{cases} \quad (47)$$

where $\tilde{\beta}_1$ and $\tilde{\beta}_2$ are the unknown parameters to be estimated for the inverse problem in the Navier–Stokes equation. The loss function for the pre-training phase of DG-PINNs is formulated by

$$\mathcal{L}_d(\boldsymbol{\theta}) = \mathcal{L}_{d1}(\boldsymbol{\theta}) + \mathcal{L}_{d2}(\boldsymbol{\theta}), \quad (48)$$

where

$$\mathcal{L}_{d1}(\boldsymbol{\theta}) = \frac{1}{N_d} \sum_{k=1}^{N_d} \left(\hat{u}(x_d^k, y_d^k, t_d^k; \boldsymbol{\theta}) - u(x_d^k, y_d^k, t_d^k) \right)^2, \quad (49)$$

and

$$\mathcal{L}_{d2}(\boldsymbol{\theta}) = \frac{1}{N_d} \sum_{k=1}^{N_d} \left(\hat{v}(x_d^k, y_d^k, t_d^k; \boldsymbol{\theta}) - v(x_d^k, y_d^k, t_d^k) \right)^2. \quad (50)$$

Then, the loss function for the fine-tuning phase of DG-PINNs is formulated by

$$\mathcal{L}(\Theta) = \lambda_{r1}\mathcal{L}_{r1}(\Theta) + \lambda_{r2}\mathcal{L}_{r2}(\Theta) + \lambda_{r3}\mathcal{L}_{r3}(\theta) + \lambda_{d1}\mathcal{L}_{d1}(\theta) + \lambda_{d2}\mathcal{L}_{d2}(\theta), \quad (51)$$

where

$$\mathcal{L}_{r1}(\Theta) = \frac{1}{N_r} \sum_{k=1}^{N_r} (f(x_r^k, y_r^k, t_r^k; \Theta))^2, \quad (52)$$

$$\mathcal{L}_{r2}(\Theta) = \frac{1}{N_r} \sum_{k=1}^{N_r} (g(x_r^k, y_r^k, t_r^k; \Theta))^2, \quad (53)$$

and

$$\mathcal{L}_{r3}(\theta) = \frac{1}{N_r} \sum_{k=1}^{N_r} (h(x_r^k, y_r^k, t_r^k; \theta))^2. \quad (54)$$

To conduct a sensitivity analysis on M_1 for the Navier–Stokes equation, fifteen DG-PINN models are trained with the same M_1 values as those specified in the sensitivity analysis on M_1 for the heat equation. The accuracy of the predictions from the fifteen DG-PINN models is evaluated by \mathcal{R}_t shown in Fig. 9(a). It can be seen that the values of \mathcal{R}_t remain below 2×10^{-2} for $v(x, y, t)$ and below 6×10^{-3} for $u(x, y, t)$. Besides, the APE between $\tilde{\beta}_1$ versus β_1 and $\tilde{\beta}_2$ versus β_2 for each DG-PINN model is shown in Figure 9(b). It is shown that the maximum APE between $\tilde{\beta}_1$ and β_1 is less than 0.3% for each M_1 and the maximum APE between $\tilde{\beta}_2$ and β_2 is less than 5% for each M_1 . In Figs. 9(c) and (d), the observed pressure field $p(x, y, t)$ and predicted pressure field $\hat{p}(x, y, t; \theta)$ at $t = 1$ with mean centering are very similar. Mean centering is used because only the gradient of the pressure field drives the Navier–Stokes equation, such that it remains unchanged with the addition of a constant to the pressure field. It can be seen that the DG-PINN can solve the inverse problem of the Navier–Stokes equation accurately even with a large range of M_1 . These results emphasize the robustness of the selection of M_1 for DG-PINNs.

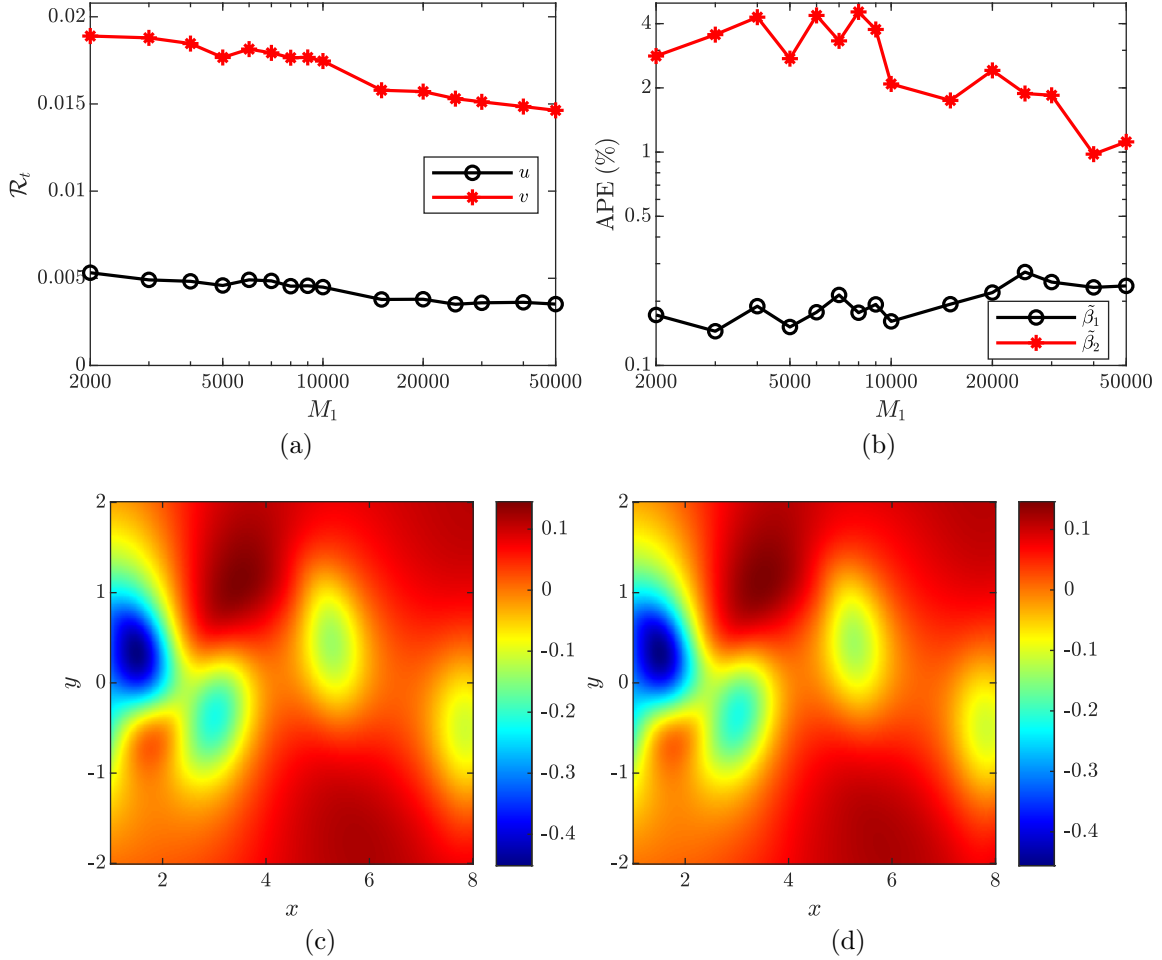


Figure 9: Sensitivity analysis on M_1 for the Navier–Stokes equation: (a) the relative L^2 errors between the testing data and the corresponding predictions of the DG-PINN models, (b) the absolute percentage error (APE) for $\tilde{\beta}_1$ versus β_1 and $\tilde{\beta}_2$ versus β_2 , (c) the observed pressure field $p(x, y, t)$ at $t = 1$, and (d) the predicted pressure field $\hat{p}(x, y, t; \theta)$ at $t = 1$.

To conduct a sensitivity analysis on N_d , fifteen DG-PINN models are trained using training datasets for $\mathcal{L}_{d1}(\theta)$ and $\mathcal{L}_{d2}(\theta)$ in the Navier–Stokes equation, with N_d values matching those used in the sensitivity analysis for the heat equation. Figure 10(a) shows that the values of \mathcal{R}_t remain below 2×10^{-2} for $v(x, y, t)$ and below 5×10^{-3} for $u(x, y, t)$. Besides, the APE between $\tilde{\beta}_1$ versus β_1 and $\tilde{\beta}_2$ versus β_2 for each DG-PINN model is shown in Figure 10(b). It is shown that the maximum APE between $\tilde{\beta}_1$ and β_1 is less than 0.3% for each N_d and the maximum APE between $\tilde{\beta}_2$ and β_2 is less than 2.6% for each N_d . In Figs. 10(c) and (d), the observed pressure field $p(x, y, t)$ and predicted pressure field $\hat{p}(x, y, t; \theta)$ at $t = 1$ with mean centering are very similar. It can be seen

that DG-PINNs can solve the inverse problem of the Navier–Stokes equation accurately even with the wide range of N_d . These results highlights the robustness of the selection of N_d for DG-PINNs.

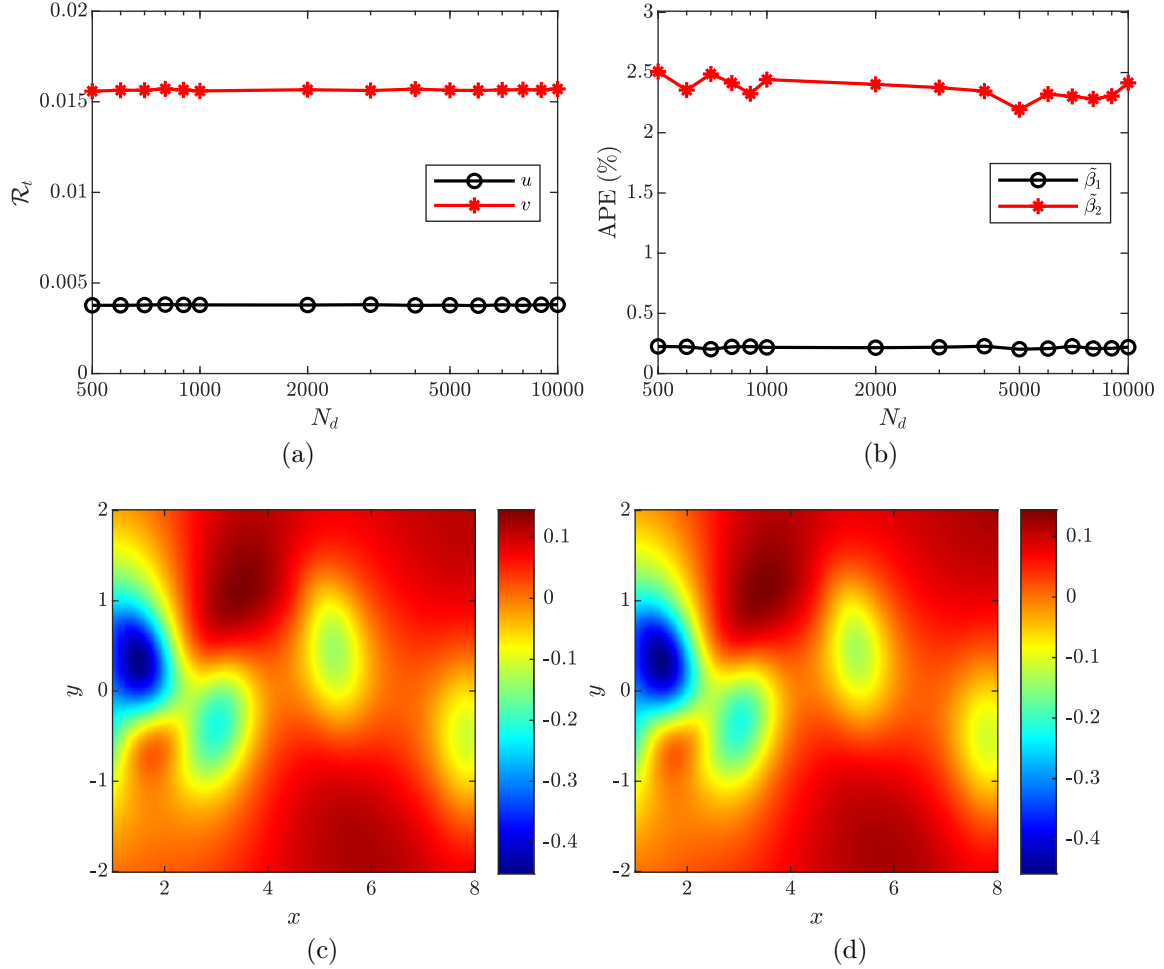


Figure 10: Sensitivity analysis on N_d for the Navier–Stokes equation: (a) the relative L^2 errors between the testing data and the corresponding predictions of the DG-PINN models, (b) the absolute percentage error (APE) for $\tilde{\beta}_1$ versus β_1 and $\tilde{\beta}_2$ versus β_2 , (c) the observed pressure field $p(x, y, t)$ at $t = 1$, and (d) the predicted pressure field $\hat{p}(x, y, t; \theta)$ at $t = 1$.

To investigate the noise-robustness of DG-PINNs for the Navier–Stokes equation, two DG-PINN models are trained using observed data contaminated with white Gaussian noise at SNRs of 40 and 35 dB, respectively. The relative L^2 errors \mathcal{R}_t for $u(x, y, t)$ are calculated as 5.70×10^{-3} and 1.06×10^{-2} for SNRs of 40 and 35 dB, respectively. Similarly, for $v(x, y, t)$, \mathcal{R}_t is calculated as 2.14×10^{-2} and 3.80×10^{-2} for SNRs of 40 and 35 dB, respectively. Besides, the APE between $\tilde{\beta}_1$ and β_1 is calculated as 0.076% and 0.22% for

SNRs of 40 and 35 dB, respectively, and the APE between $\tilde{\beta}_2$ and β_2 is calculated as 0.136% and 8.89% for SNRs of 40 and 35 dB, respectively. These results indicate that DG-PINNs are capable of solving the inverse problem of the Navier–Stokes equation in the presence of noise contamination. However, the accuracy of β_2 estimation is more sensitive to noise, with a substantial decrease in precision as the noise level increases.

To evaluate the efficiency of PINNs and DG-PINNs, both approaches are applied in ten independent trials to solve the inverse problem of the Navier–Stokes equation. The averaged \mathcal{R}_t , APE, and training time are listed in Table 4. It is shown that both \mathcal{R}_t for $u(x, y, t)$ and $v(x, y, t)$ in DG-PINNs are lower than those in PINNs, indicating that DG-PINNs provide more accurate predictions compared to PINNs. Regarding the APE for $\tilde{\beta}_1$ versus β_1 and $\tilde{\beta}_2$ versus β_2 , DG-PINNs exhibit a smaller error compared to PINNs, indicating that DG-PINNs provide a more accurate estimation of β_1 and β_2 . Besides, the training time for DG-PINNs is significantly shorter than that for PINNs. These results demonstrate that DG-PINNs are around nine times faster than PINNs in solving the inverse problem of the Navier–Stokes equation, achieving higher accuracy in both predictions and the estimation of β_1 and β_2 .

Table 4: Results of the comparative analysis between DG-PINNs and PINNs for the Navier–Stokes equation.

Method	\mathcal{R}_t		APE		Training time
	$u(x, y, t)$	$v(x, y, t)$	$\tilde{\beta}_1$	$\tilde{\beta}_2$	
PINN	1.45×10^{-2}	6.17×10^{-2}	0.32%	13.83%	58.12 min
DG-PINN	4.17×10^{-3}	1.66×10^{-2}	0.27%	2.29%	6.80 min

4. Concluding Remarks

In this study, a novel framework for solving inverse problems in PDEs, referred to as the data-guided physics-informed neural networks (DG-PINNs), is proposed. The DG-PINNs framework is structured two phases: a pre-training phase and a fine-tuning phase. In the pre-training phase, a neural network is trained to minimize the data loss.

While in the fine-tuning phase, the neural network is further optimized by integrating fundamental physical laws into its loss function. The effectiveness, noise-robustness, and efficiency of DG-PINNs in solving inverse problems of PDEs are validated through a series of numerical investigations on various PDEs, including the heat equation, wave equation, Euler–Bernoulli beam equation and Navier–Stokes equation. For each equation, sensitivity analyses of the DG-PINNs results are conducted focusing on two hyperparameters: the maximum number of iterations in the pre-training phase and the number of data points for the data loss. These sensitivity analyses not only reveal the effectiveness of DG-PINNs in accurately solving inverse problems in PDEs but also underscore the robustness of the selection of these hyperparameters. Besides, investigations of noise-robustness show that DG-PINNs are capable of accurately solving inverse problems in PDEs in the presence of noise contamination. Furthermore, results from the comparative analysis between DG-PINNs and PINNs show that DG-PINNs offer a significant computational advantage over PINNs, demonstrating faster computation times while maintaining high accuracy in the solution. In future work, it would be valuable to explore the application of DG-PINNs to a wider range of physical phenomena. It is worth noting that the two-phase framework can be extended to physics-informed neural operators.

Acknowledgments

The authors are grateful for the financial support from the National Science Foundation through Grant No. CMMI-1762917.

Conflicts of Interest

The authors declare no conflict of interest.

References

- [1] G. E. Karniadakis, I. G. Kevrekidis, L. Lu, P. Perdikaris, S. Wang, L. Yang, Physics-informed machine learning, *Nature Reviews Physics* 3 (6) (2021) 422–440.

- [2] M. Raissi, P. Perdikaris, G. E. Karniadakis, Physics-informed neural networks: A deep learning framework for solving forward and inverse problems involving nonlinear partial differential equations, *Journal of Computational Physics* 378 (2019) 686–707.
- [3] K. Hornik, M. Stinchcombe, H. White, Multilayer feedforward networks are universal approximators, *Neural Networks* 2 (5) (1989) 359–366.
- [4] A. G. Baydin, B. A. Pearlmutter, A. A. Radul, J. M. Siskind, Automatic differentiation in machine learning: a survey, *Journal of Machine Learning Research* 18 (153) (2018) 1–43.
- [5] H. Lee, I. S. Kang, Neural algorithm for solving differential equations, *Journal of Computational Physics* 91 (1) (1990) 110–131.
- [6] M. Dissanayake, N. Phan-Thien, Neural-network-based approximations for solving partial differential equations, *Communications in Numerical Methods in Engineering* 10 (3) (1994) 195–201.
- [7] A. J. Meade Jr, A. A. Fernandez, Solution of nonlinear ordinary differential equations by feedforward neural networks, *Mathematical and Computer Modelling* 20 (9) (1994) 19–44.
- [8] M. Raissi, A. Yazdani, G. E. Karniadakis, Hidden fluid mechanics: Learning velocity and pressure fields from flow visualizations, *Science* 367 (6481) (2020) 1026–1030.
- [9] Z. Mao, A. D. Jagtap, G. E. Karniadakis, Physics-informed neural networks for high-speed flows, *Computer Methods in Applied Mechanics and Engineering* 360 (2020) 112789.
- [10] X. Jin, S. Cai, H. Li, G. E. Karniadakis, Nsfnets (navier-stokes flow nets): Physics-informed neural networks for the incompressible navier-stokes equations, *Journal of Computational Physics* 426 (2021) 109951.
- [11] D. Fang, J. Tan, Immersed boundary-physics informed machine learning approach for fluid–solid coupling, *Ocean Engineering* 263 (2022) 112360.

- [12] K. Shukla, P. C. Di Leoni, J. Blackshire, D. Sparkman, G. E. Karniadakis, Physics-informed neural network for ultrasound nondestructive quantification of surface breaking cracks, *Journal of Nondestructive Evaluation* 39 (3) (2020) 1–20.
- [13] E. Haghighat, M. Raissi, A. Moure, H. Gomez, R. Juanes, A physics-informed deep learning framework for inversion and surrogate modeling in solid mechanics, *Computer Methods in Applied Mechanics and Engineering* 379 (2021) 113741.
- [14] W. Zhou, Y. Xu, Damage identification for beam-like structures based on physics-informed neural networks, in: *Society for Experimental Mechanics Annual Conference and Exposition*, Springer, 2023, pp. 1–11.
- [15] W. Zhou, Y. Xu, Damage identification for plate structures using physics-informed neural networks, *Mechanical Systems and Signal Processing* 209 (2024) 111111.
- [16] G. Kissas, Y. Yang, E. Hwuang, W. R. Witschey, J. A. Detre, P. Perdikaris, Machine learning in cardiovascular flows modeling: Predicting arterial blood pressure from non-invasive 4d flow mri data using physics-informed neural networks, *Computer Methods in Applied Mechanics and Engineering* 358 (2020) 112623.
- [17] Z. Fang, J. Zhan, Deep physical informed neural networks for metamaterial design, *IEEE Access* 8 (2019) 24506–24513.
- [18] Y. Chen, L. Lu, G. E. Karniadakis, L. Dal Negro, Physics-informed neural networks for inverse problems in nano-optics and metamaterials, *Optics Express* 28 (8) (2020) 11618–11633.
- [19] W. Ji, W. Qiu, Z. Shi, S. Pan, S. Deng, Stiff-pinn: Physics-informed neural network for stiff chemical kinetics, *The Journal of Physical Chemistry A* 125 (36) (2021) 8098–8106.
- [20] X.-Y. Guo, S.-E. Fang, Structural parameter identification using physics-informed neural networks, *Measurement* 220 (2023) 113334.

- [21] S. Wang, Y. Teng, P. Perdikaris, Understanding and mitigating gradient flow pathologies in physics-informed neural networks, *SIAM Journal on Scientific Computing* 43 (5) (2021) A3055–A3081.
- [22] N. Rahaman, A. Baratin, D. Arpit, F. Draxler, M. Lin, F. Hamprecht, Y. Bengio, A. Courville, On the spectral bias of neural networks, in: *International Conference on Machine Learning*, PMLR, 2019, pp. 5301–5310.
- [23] Z.-Q. J. Xu, Y. Zhang, T. Luo, Y. Xiao, Z. Ma, Frequency principle: Fourier analysis sheds light on deep neural networks, *arXiv preprint arXiv:1901.06523* (2019).
- [24] S. Wang, H. Wang, P. Perdikaris, On the eigenvector bias of Fourier feature networks: From regression to solving multi-scale PDEs with physics-informed neural networks, *Computer Methods in Applied Mechanics and Engineering* 384 (2021) 113938.
- [25] S. Wang, X. Yu, P. Perdikaris, When and why pinns fail to train: A neural tangent kernel perspective, *Journal of Computational Physics* 449 (2022) 110768.
- [26] A. Jacot, F. Gabriel, C. Hongler, Neural tangent kernel: Convergence and generalization in neural networks, *Advances in Neural Information Processing Systems* 31 (2018).
- [27] X. Li, Y. Liu, Z. Liu, Physics-informed neural network based on a new adaptive gradient descent algorithm for solving partial differential equations of flow problems, *Physics of Fluids* 35 (6) (2023).
- [28] M. Tancik, P. Srinivasan, B. Mildenhall, S. Fridovich-Keil, N. Raghavan, U. Singhal, R. Ramamoorthi, J. Barron, R. Ng, Fourier features let networks learn high frequency functions in low dimensional domains, *Advances in Neural Information Processing Systems* 33 (2020) 7537–7547.
- [29] C. Song, Y. Wang, Simulating seismic multifrequency wavefields with the fourier feature physics-informed neural network, *Geophysical Journal International* 232 (3) (2023) 1503–1514.

- [30] J. C. Wong, C. Ooi, A. Gupta, Y.-S. Ong, Learning in sinusoidal spaces with physics-informed neural networks, *IEEE Transactions on Artificial Intelligence* (2022).
- [31] L. Lu, X. Meng, Z. Mao, G. E. Karniadakis, Deepxde: A deep learning library for solving differential equations, *SIAM Review* 63 (1) (2021) 208–228.
- [32] P.-H. Chiu, J. C. Wong, C. Ooi, M. H. Dao, Y.-S. Ong, Can-pinn: A fast physics-informed neural network based on coupled-automatic–numerical differentiation method, *Computer Methods in Applied Mechanics and Engineering* 395 (2022) 114909.
- [33] A. D. Jagtap, K. Kawaguchi, G. E. Karniadakis, Adaptive activation functions accelerate convergence in deep and physics-informed neural networks, *Journal of Computational Physics* 404 (2020) 109136.
- [34] V. Dwivedi, B. Srinivasan, Physics informed extreme learning machine (pielm)—a rapid method for the numerical solution of partial differential equations, *Neurocomputing* 391 (2020) 96–118.
- [35] S. Basir, I. Senocak, Physics and equality constrained artificial neural networks: application to forward and inverse problems with multi-fidelity data fusion, *Journal of Computational Physics* 463 (2022) 111301.
- [36] Y.-H. Tseng, T.-S. Lin, W.-F. Hu, M.-C. Lai, A cusp-capturing pinn for elliptic interface problems, *Journal of Computational Physics* 491 (2023) 112359.
- [37] L. D. McClenny, U. M. Braga-Neto, Self-adaptive physics-informed neural networks, *Journal of Computational Physics* 474 (2023) 111722.
- [38] L. Lu, R. Pestourie, W. Yao, Z. Wang, F. Verdugo, S. G. Johnson, Physics-informed neural networks with hard constraints for inverse design, *SIAM Journal on Scientific Computing* 43 (6) (2021) B1105–B1132.
- [39] E. Zhang, M. Dao, G. E. Karniadakis, S. Suresh, Analyses of internal structures and

- defects in materials using physics-informed neural networks, *Science Advances* 8 (7) (2022) eabk0644.
- [40] M. Rasht-Behesht, C. Huber, K. Shukla, G. E. Karniadakis, Physics-informed neural networks (pinns) for wave propagation and full waveform inversions, *Journal of Geophysical Research: Solid Earth* 127 (5) (2022) e2021JB023120.
- [41] C. Xu, B. T. Cao, Y. Yuan, G. Meschke, Transfer learning based physics-informed neural networks for solving inverse problems in engineering structures under different loading scenarios, *Computer Methods in Applied Mechanics and Engineering* 405 (2023) 115852.
- [42] Z. Xiang, W. Peng, X. Liu, W. Yao, Self-adaptive loss balanced physics-informed neural networks, *Neurocomputing* 496 (2022) 11–34.
- [43] Q. He, D. Barajas-Solano, G. Tartakovsky, A. M. Tartakovsky, Physics-informed neural networks for multiphysics data assimilation with application to subsurface transport, *Advances in Water Resources* 141 (2020) 103610.
- [44] S. Cuomo, V. S. Di Cola, F. Giampaolo, G. Rozza, M. Raissi, F. Piccialli, Scientific machine learning through physics-informed neural networks: Where we are and what’s next, *Journal of Scientific Computing* 92 (3) (2022) 88.
- [45] W. Chen, Q. Wang, J. S. Hesthaven, C. Zhang, Physics-informed machine learning for reduced-order modeling of nonlinear problems, *Journal of computational Physics* 446 (2021) 110666.
- [46] D. P. Kingma, J. Ba, Adam: A method for stochastic optimization, arXiv preprint arXiv:1412.6980 (2014).
- [47] D. C. Liu, J. Nocedal, On the limited memory BFGS method for large scale optimization, *Mathematical Programming* 45 (1) (1989) 503–528.
- [48] Y. Ding, S. Chen, X. Li, L. Jin, S. Luan, H. Sun, Physics-constrained neural networks for half-space seismic wave modeling, *Computers & Geosciences* 181 (2023) 105477.

- [49] A. Paszke, S. Gross, F. Massa, A. Lerer, J. Bradbury, G. Chanan, T. Killeen, Z. Lin, N. Gimeshein, L. Antiga, et al., Pytorch: An imperative style, high-performance deep learning library, *Advances in Neural Information Processing Systems* 32 (2019).
- [50] L. C. Evans, *Partial Differential Equations: Second Edition*, 2nd Edition, Graduate Studies in Mathematics, AMS, 2010.
- [51] P. Hagedorn, A. DasGupta, *Vibrations and waves in continuous mechanical systems*, John Wiley & Sons, 2007.